Scientific Research Publishing

World Journal of Nuclear Science and Technology, 2026, 16(3), 94-119
https://www.scirp.org/journal/wjnst
ISSN Online: 2161-6809
ISSN Print: 2161-6795

Proton-Induced Reaction on ^{169}Tm up to 200 MeV and the Production of the Therapeutic Radionuclide ^{169}Yb

Sukarna Banik[1], Md. Kawchar Ahmed Patwary[1], Hasan Murad[2]

[1]Department of Physics, Comilla University, Cumilla, Bangladesh
[2]Department of Physics, Comilla Victoria College, Cumilla, Bangladesh
Email: kapphysics@cou.ac.bd

How to cite this paper: Banik, S., Patwary, M.K.A. and Murad, H. (2026) Proton-Induced Reaction on ^{169}Tm up to 200 MeV and the Production of the Therapeutic Radionuclide ^{169}Yb. *World Journal of Nuclear Science and Technology*, **16**, 94-119.
https://doi.org/10.4236/wjnst.2026.163007

Received: June 23, 2026
Accepted: July 24, 2026
Published: July 27, 2026

Abstract

A systematic theoretical investigation of proton-induced nuclear reactions on ^{169}Tm was performed using the TALYS-2.0 nuclear reaction code for incident proton energies up to 200 MeV. Excitation functions were calculated for the ^{169}Tm(p, n+α)^{165}Er, ^{169}Tm(p, α)^{166}Er, ^{169}Tm(p, ^{3}He)^{167}Er, ^{169}Tm(p, t)^{167}Tm, ^{169}Tm(p, n+p)^{168}Tm, ^{169}Tm(p, 4n)^{166}Yb, ^{169}Tm(p, 3n)^{167}Yb, ^{169}Tm(p, 2n)^{168}Yb, ^{169}Tm(p, n)^{169}Yb, and ^{169}Tm(p, γ)^{170}Yb reaction channels using six nuclear level density models (CTM, BFM, GSM, SHFB, SHFB(C), and GHFB). Particular attention was given to the medically important ^{169}Tm(p, n)^{169}Yb reaction for the production of the therapeutic radionuclide ^{169}Yb. The calculated excitation functions were compared with available experimental data from the EXFOR database and the TENDL-2023 evaluated library. Model performance was assessed through statistical deviation factors (F, D, and R), revealing that no single level density model consistently outperformed the others across all reactions and datasets. Phenomenological models generally showed better agreement with TENDL-2023 evaluations, whereas microscopic models provided improved consistency with several experimental measurements. The ^{169}Tm(p, n)^{169}Yb reaction exhibited an optimum energy region around 10 - 15 MeV, with a maximum cross section near 11 MeV. Production characteristics, including activity, production amount, and integral yield, confirmed the feasibility of accelerator-based ^{169}Yb production. The present results provide valuable nuclear data for reaction channels lacking experimental information and support the development of reliable production routes for ^{169}Yb in nuclear medicine applications.

Keywords

^{169}Tm(p, n)^{169}Yb Reaction, Therapeutic Radionuclide ^{169}Yb, TALYS-2.0,

Nuclear Level Density Models, Excitation Function

1. Introduction

Reliable nuclear reaction cross-section data are essential for a wide range of scientific and technological applications, including radionuclide production for nuclear medicine, radiation processing, industrial radiography, non-destructive testing, reactor technology, accelerator-driven systems, and nuclear data evaluation. Among accelerator-based reactions, proton-induced reactions are particularly important because they provide practical routes for producing medical radionuclides with high specific activity and minimal radioactive waste [1] [2]. Accurate excitation functions are therefore required for optimizing irradiation parameters, estimating production yields, and improving the predictive capability of nuclear reaction models.

The monoisotopic target ^{169}Tm (abundance = 100% [3]) has attracted considerable interest because proton irradiation can produce a variety of erbium, thulium, and ytterbium radionuclides through different reaction channels. Despite its importance, experimental nuclear data for proton-induced reactions on ^{169}Tm remain incomplete. Several reaction channels, including ^{169}Tm(p, n + α)^{165}Er, ^{169}Tm(p, α)^{166}Er, ^{169}Tm(p, ^{3}He)^{167}Er, ^{169}Tm(p, t)^{167}Tm, ^{169}Tm(p, n + p)^{168}Tm, ^{169}Tm(p, 2n)^{168}Yb, and ^{169}Tm(p, γ)^{170}Yb currently have no experimental cross-section data available in the EXFOR database [4]. Consequently, theoretical investigations are required to establish excitation functions and provide guidance for future measurements.

For the ^{169}Tm(p, 4n)^{166}Yb and ^{169}Tm(p, 3n)^{167}Yb reactions, experimental studies have been reported by Birattari *et al.* [5] and Tárkányi *et al.* [6] over proton energies up to approximately 45 MeV. However, noticeable discrepancies exist between the measured excitation functions, particularly in the peak cross-section region, making it difficult to establish reliable production parameters and evaluate the predictive performance of theoretical models. Such inconsistencies highlight the need for a systematic investigation using modern nuclear reaction codes and model comparisons.

Particular attention has been devoted to the ^{169}Tm(p, n)^{169}Yb reaction because it provides an accelerator-based route for producing the therapeutic radionuclide ^{169}Yb. This radionuclide ($T_{1/2}$ = 32.018 d) decays primarily by electron capture (I_{EC} = 100%) with emissions of Auger electrons, X-rays (k_{α} = 50.74 keV, 147.8%; k_{β} = 57.52 keV, 37.9%) and emits low-energy photons [3] suitable for brachytherapy as a potential substitute for ^{125}I and ^{192}Ir, image-guided therapy, and other therapeutic applications [7]-[11]. Owing to its favorable decay characteristics, relatively long half-life, and established clinical use in radiation therapy, ^{169}Yb continues to attract interest as a medically relevant radionuclide [12]-[14]. The excitation function of the ^{169}Tm(p, n)^{169}Yb reaction was first investigated by Birattari *et al.* [5]

over the proton energy range of 5 - 45 MeV. Subsequently, Spahn *et al.* [15] measured the reaction cross section up to 45 MeV using the stacked-foil technique and high-resolution γ-ray spectrometry and reported an integral yield of approximately 1.5 MBq/mA-h within the optimum energy range of 7 - 16 MeV. Later, Tárkányi *et al.* [6] extended the investigation of proton-induced reactions on ^{169}Tm in the energy range of 24.5 - 35.8 MeV using stacked-foil activation and high-resolution γ-ray spectroscopy. More recently, Saito *et al.* [16] measured the excitation function from 5.3 to 17.5 MeV and provided detailed low-energy cross-section data that clearly describe the reaction threshold and peak region. However, significant discrepancies remain between the datasets reported by Saito *et al.* [16] and Spahn *et al.* [15], particularly within the proton energy range of 10 - 20 MeV. These differences emphasize the need for a comprehensive evaluation of proton-induced reactions on ^{169}Tm and a systematic assessment of the associated nuclear reaction models.

In the present study, TALYS-2.0 [17] was employed to investigate proton-induced reactions on ^{169}Tm over the energy range from reaction threshold to 200 MeV. Six nuclear level density models, namely the Constant Temperature Model (CTM), Back-Shifted Fermi Gas Model (BFM), Generalized Superfluid Model (GSM), Skyrme-Hartree-Fock-Bogoliubov (SHFB), Combinatorial SHFB (SHFB(C)), and Gogny-Hartree-Fock-Bogoliubov (GHFB), were considered to evaluate their influence on the calculated excitation functions. In addition to cross-section calculations, the production of the therapeutic radionuclide ^{169}Yb through the ^{169}Tm(p, n)^{169}Yb reaction was investigated by estimating activity, production amount, and yield. The validity of the employed nuclear models was assessed through statistical deviation factor analysis using the *F*-, *D*-, and *R*-factors, allowing direct comparison between theoretical predictions, experimental measurements retrieved from the EXFOR database [4], and evaluated TENDL-2023 nuclear data library [18]. The results provide new insights into proton-induced reactions on ^{169}Tm, contribute to the improvement of nuclear data evaluations, and support the development of accelerator-based production routes for medically important radionuclides ^{169}Yb.

2. Materials and Methodology

2.1. TALYS-2.0

The theoretical calculations in this study were performed using TALYS-2.0, a comprehensive nuclear reaction code developed for the analysis and prediction of nuclear reactions through an optimized integration of established nuclear models [17]. TALYS has been widely applied in the interpretation of experimental nuclear reaction data and the generation of evaluated nuclear data for scientific, medical, and technological applications. The code is capable of simulating neutron-, photon-, proton-, deuteron-, triton-, ^{3}He-, and α-particle-induced reactions over an incident energy range of 0.001 - 200 MeV. In the present work, TALYS-2.0 was employed to perform a continuous evaluation of the excitation functions of the

^{169}Tm(p, x) reaction channels up to 200 MeV. The nuclear decay characteristics and Q-values of the possible contributing reaction channels were obtained from the National Nuclear Data Center (NNDC) database [3] [19] and are summarized in Table 1.

Table 1. Decay characteristics of the investigated reaction products [3] [19].

Nuclide	Half-life	E_γ (keV)	I_γ (keV)	Reaction channel	Q-value (keV)	Threshold (keV)
^{165}Er	10.3 h	46.7	21,500	^{169}Tm(p, n + α)	39.44	0
		47.547	37,900			
		53.877	7730			
		6.72	17,000			
^{166}Er	Stable	------	-----	^{169}Tm(p, α)	8513.5	0
^{167}Er	2.269 s	48.221	5400	^{169}Tm(p, ^{3}He)	−5627.6	5661.2
		49.128	9500			
		207.801	42,400			
^{167}Tm	9.25 d	48.221	27,000	^{169}Tm(p, t)	−6392.4	6430.5
		49.128	48,000			
		207.801	41,300			
^{168}Tm	93.1 d	184.295	18,150	^{169}Tm(p, n + p)	−8033.6	8081.5
		198.251	54,490			
		447.515	23,980			
		631.705	9260			
		720.392	12206.8			
		741.355	12,810			
		815.989	50,950			
		821.162	11,990			
^{166}Yb	56.7 h	50.742	69,000	^{169}Tm(p, 4n)	−24677	24824
		82.29	15,550			
^{167}Yb	17.5 m	106.162	22,900	^{169}Tm(p, 3n)	−17610	17715
		113.32	56,200			
		176.23	20,800			
		177.22	2770			
^{168}Yb	Stable	-----	------	^{169}Tm(p, 2n)	−8548.5	8599.4
^{169}Yb	32.018 d	109.779	17,390	^{169}Tm(p, n)	−1681.5	1691.5
		130.523	11,380			
		177.213	22,280			
		197.956	35,930			
		307.735	10,500			
^{170}Yb	Stable	------	------	^{169}Tm(p, γ)	67778.2	0

The sensitivity analysis presented in this work is focused primarily on the role of nuclear level densities. While the nuclear level density model (LDM) was systematically varied across six distinct frameworks, the optical model potentials (OMP) and pre-equilibrium parameters were maintained at their global default settings. Consequently, the observed variations reflect the isolated model dependence on level densities alone, providing a focused baseline for the proton-induced reaction channel.

2.1.1. Optical Model Parameters

In TALYS-2.0, reaction cross-sections are calculated within the Hauser-Feshbach statistical theory, where the optical model potential (OMP) and nuclear level density play fundamental roles in describing the reaction mechanism. The OMP is essential for predicting key nuclear reaction observables, including elastic, inelastic, and total reaction cross-sections, angular distributions, and transmission coefficients that govern compound nucleus decay and pre-equilibrium particle emission through either deformed nuclear potentials or distorted-wave Born approximation (DWBA)-based approaches [18]. In TALYS, optical model calculations are performed using the ECIS-06 code developed by Raynal [20]. The default proton optical model parameters implemented in TALYS-2.0 are based on the local and global parameterizations proposed by Koning and Delaroche [21]. For proton-induced reactions, the energy dependence of the potential depths is described as a function of ($E-E_f^p$), where E is the incident proton energy and E_f^p, denotes the proton Fermi energy, defined as the energy midway between the last occupied and the first unoccupied nuclear shell states. For incident protons,

$$E_f^p = -\frac{1}{2}\left[S_p(Z,N) + S_p(Z+1,N)\right], \tag{1}$$

where S_p is the proton separation energy with Z being the proton number. The nuclear structure mass tables implemented in TALYS-2.0 are used to determine the particle separation energies required for reaction calculations.

The optical model parameterization for incident proton is given by Equations (2) to (6).

$$V_V(E) = v_1\left[1 - v_2\left(E-E_f^p\right) + v_3\left(E-E_f^p\right)^2 - v_4\left(E-E_f^p\right)^3\right], \tag{2}$$

$$W_V(E) = w_1\frac{\left(E-E_f^p\right)^2}{\left(E-E_f^p\right)^2 + \left(w_2\right)^2}, \tag{3}$$

$$W_D(E) = d_1\frac{\left(E-E_f^p\right)^2}{\left(E-E_f^p\right)^2 + \left(d_2\right)^2}\exp\left[-d_2\left(E-E_f^p\right)\right], \tag{4}$$

$$V_{SO}(E) = v_{SO,1}\exp\left[-v_{SO,2}\left(E-E_f^p\right)\right], \tag{5}$$

$$W_{SO}(E) = w_{SO,1}\frac{\left(E-E_f^p\right)^2}{\left(E-E_f^p\right)^2 + \left(w_{SO,2}\right)^2}. \tag{6}$$

Here, V_V and V_{SO} denote the real components of the volume-central (V) and spin-orbit (SO) potentials, whereas W_V, W_D, W_{SO} represent the corresponding imaginary components associated with the volume-central (V), surface-central (D) and spin-orbit (SO) terms, respectively. The variable E denotes the incident proton energy in the laboratory reference frame, with the model being applicable over the energy range of 0.001 - 200 MeV. In TALYS-2.0, the local optical model parameters (e.g., v_1, v_2, and related coefficients) are automatically retrieved from the built-in nuclear structure and model parameter database [21].

2.1.2. Mass Model

Nuclear mass models play a fundamental role in cross-section calculations, as particle separation energies and Q-values are directly determined by the masses of the participating nuclides and dictate the energetic feasibility of individual reaction channels. TALYS-2.0 provides four nuclear mass model options for reaction calculations [17].

In the present study, the GHFB [22] mass model was adopted for the reaction calculations. The GHFB approach is a microscopic nuclear structure model based on self-consistent mean-field theory using the Gogny effective interaction. One of its important advantages is the explicit treatment of nuclear deformation and quadrupole correlation energies within the framework of the 5D collective Hamiltonian approach. Owing to its strong theoretical foundation and reliable predictive performance, the GHFB mass model was selected in the present work to achieve more accurate calculations of the reaction cross-sections and production characteristics.

2.1.3. Nuclear Level Density Model

Nuclear level density models (LDMs) are essential in statistical reaction calculations, as they significantly influence the prediction of reaction cross-sections, radionuclide yields, and production optimization. TALYS-2.0 provides six LDMs for reaction analysis [17]. The phenomenological models include CTM, BFM, and GSM, all derived from the Fermi Gas Model (FGM), which assumes uniformly spaced single-particle energy levels without explicit consideration of collective excitations. The microscopic approaches consist of the SHFB, SHFB(C), and GHFB model. In the present study, all six LDMs available in TALYS-2.0 were systematically investigated to evaluate their influence on the cross-section profiling of the ^{169}Tm(p, x) reaction.

The level density, $\rho\left(E_x, J, \Pi\right)$ represents the number of nuclear levels per MeV around an excitation energy E_x, for a certain spin J and parity Π. The total level density $\rho^{tot}\left(E_x\right)$ yields the total number of levels per MeV around E_x which is obtained by summing over J and Π, as shown in Equation (7).

$$\rho^{tot}\left(E_x\right) = \sum_{J}\sum_{\Pi}\rho\left(E_x, J, \Pi\right) \tag{7}$$

1) Phenomenological Level Density Models

a) Constant Temperature Model (CTM)

The CTM is a phenomenological level density model in which an effective temperature, T, is introduced to describe the exponential dependence of level density on excitation energy within the shell-model framework [23]. Owing to its simplicity and reliable performance in the low-excitation energy region, the CTM has been widely employed in nuclear reaction calculations. Although the model provides an effective description of nuclear level densities at lower excitation energies, its applicability gradually decreases at higher excitation energies. The model, originally proposed by Gilbert and Cameron [24], divides E_x, into two regions separated by a matching energy, E_M. For E_x below E_M, the total level density is described by the constant temperature formalism, whereas above E_M, the level density is represented by the Fermi-gas approximation [17]. Accordingly, for $0 < E_x \le E_M$, the total level density is expressed as shown in Equation (8a):

$$\rho^{tot}\left(E_x\right) = \rho_T^{tot}\left(E_x\right), \text{ if } \; 0 < E_x \le E_M \tag{8a}$$

Above E_M, it is given by Equation (8b):

$$\rho^{tot}\left(E_x\right) = \rho_F^{tot}\left(E_x\right), \text{ if } \; E_x \ge E_M . \tag{8b}$$

b) Back-Shifted Fermi Gas Model (BFM)

Although the conventional FGM provides a useful framework for describing nuclear level densities, it has several inherent limitations, particularly in accounting for pairing correlations and low-energy nuclear structure effects. Nevertheless, owing to its simplicity and its ability to reproduce systematic trends in experimental level density data through fits to cumulative low-lying discrete states and the average spacing of *s*-wave neutron resonances near the neutron binding energy, the FGM remains widely used in nuclear reaction studies [25].

To overcome these limitations, the BFM, originally developed by Dilg *et al.* [26], introduces an adjustable back-shift parameter to incorporate pairing effects into the excitation energy. This modification allows the standard Fermi gas formalism to be extended smoothly down to zero effective excitation energy, U, thereby providing a simple treatment of pairing correlations. However, the original formulation exhibits singular behavior as the effective excitation energy approaches zero. To address this issue, an improved treatment was first proposed by Grossjean and Feldmeier [27], and later reformulated into a practical implementation by Demetriou and Goriely [28], which has subsequently been adopted in the TALYS nuclear reaction code. Accordingly, the total level density is expressed by Equation (9).

$$\rho_{BFM}^{tot}\left(E_x\right) = \left[\frac{1}{\rho_F^{tot}\left(E_x\right)} + \frac{1}{\rho_0\left(t\right)}\right]^{-1}, \tag{9}$$

where $\rho_0\left(t\right)$ is the scaling prefactor of the Fermi-gas formula, determined by the level density parameter a and the energy shift Δ, which anchors the model to experimental data.

c) Generalized Superfluid Model (GSM)

The GSM, introduced by Ignatyuk *et al.* [29] [30], extends the conventional FGM by explicitly incorporating pairing correlations through the Bardeen-Cooper-Schrieffer theory, treating nuclei as superfluid systems at low excitation energies. In this framework, nucleon pairs reduce the level density compared with that predicted by the normal Fermi gas approximation. As excitation energy increases, these pairing correlations gradually diminish, and the model transitions smoothly to the standard FGM description. The GSM describes the nuclear level density using two distinct formulations: one corresponding to the paired (superfluid) phase below critical excitation energy U_c, and the other corresponding to the unpaired (normal) phase above U_c. This treatment provides a more physically realistic representation of nuclear structure effects than the CTM or BFM, as it explicitly models the phase transition from superfluid to normal nuclear matter. For excitation energy $U \le U_c$, the total level density is expressed by Equation (10).

$$\rho_{BFM}^{tot}\left(E_x\right) = \frac{1}{\sqrt{2\pi}\sigma}\frac{\mathrm{e}^S}{\sqrt{D}}, \tag{10}$$

where S is the entropy and D is the determinant related to the saddle-point approximation.

2) Microscopic Level Density Models

In the Reference Input Parameter Library (RIPL) [31], Goriely has provided an extensive set of microscopic nuclear level densities based on the SHFB model, covering nuclei across the entire nuclear chart, from the proton drip line to the neutron drip line. These level densities were obtained through Hartree-Fock-based calculations for excitation energies up to 150 MeV [32]. Moreover, Hilaire and Goriely [33] have introduced energy-, spin-, and parity-dependent nuclear level densities based on a microscopic combinatorial approach called SHFB(C). In this model, the intrinsic state density is calculated explicitly from single-particle configurations, while collective effects, including rotational and vibrational enhancements, are incorporated in detail and self-consistent manner. The most recent microscopic level density option implemented in TALYS is the GHFB model, which is based on temperature-dependent Hartree-Fock-Bogoliubov calculations using the Gogny effective nucleon–nucleon interaction [34]. Unlike phenomenological approaches, these microscopic level densities, ρ_{HFM}, are derived directly from nuclear structure calculations and are not adjusted to experimental data. To improve flexibility in fitting experimental observables, TALYS-2.0 introduces an additional scaling function for these microscopic models. Accordingly, the level density for the microscopic models is expressed by Equation (11).

$$\rho\left(E_x, J, \Pi\right) = \exp\left(c\sqrt{E_x - \delta}\right)\rho_{HFM}\left(E_x - \delta, J, \Pi\right) \tag{11}$$

In Equation (11), the scaling constant, c, and the pairing shift parameter, δ, are set to their default values of $c = 0$ and $\delta = 0$ in TALYS-2.0. These parameters serve roles analogous to those used in phenomenological level density models. The parameter δ corresponds to the back-shift parameter, Δ, in the BFM, intro-

ducing an effectively shift in excitation energy to account for pairing correlations and odd-even nuclear effects. Similarly, the parameter c plays a role comparable to the level density parameter, a, in the BFM, controlling the overall magnitude and energy dependence of the level density at higher excitation energy region.

2.2. Target Design

For the cross-section calculations, a ^{169}Tm foil was selected as the target material in TALYS-2.0 to evaluate the excitation functions of proton-induced reactions on ^{169}Tm for all possible reaction channels up to an incident proton energy of 200 MeV. The target geometry was defined as 0.03353 mm^{t} × 10 mm × 10 mm [16] [35]. The GHFB mass model [22] was adopted in the TALYS-2.0 calculations. The primary nuclear model parameters in the TALYS calculation, including the pre-equilibrium model, gamma-emission functions, and width-fluctuation corrections were maintained at their default TALYS-2.0 values. A flag was enforced to incorporate spherical Optical Model in the TALYS 2.0 input parameters. Cross-section profiling was performed using all six available LDMs to systematically investigate model-dependent variations in the predicted reaction channels. Furthermore, for radionuclide production assessment using the calculated cross section data, the proton beam current was fixed at 5 mA with an irradiation period of 24 h, followed by a cooling period of 24 h. In addition, the activity, production amount, and integral yield of ^{169}Yb were evaluated for the ^{169}Tm(p, n)^{169}Yb reaction to assess the feasibility of accelerator-based production of this medically relevant radionuclide.

2.3. Validation of the Nuclear Model

To validate the nuclear models, statistical factor analyses were performed to quantitatively assess the variation among the LDMs and their agreement with the experimental cross-section data for the proton-induced reaction on ^{169}Tm, as available in the EXFOR database [4].

Three statistical deviation factors were chosen to analyze the predictive reliability of the LDMs [36]-[38]. These are:

1) Mean deviation: F-factor (F = 1: perfect agreement)

$$F = 10^{\sqrt{\frac{1}{N}\sum_{i=1}^{N}\left(\log\sigma_i^{exp}-\log\sigma_i^{cal}\right)^2}} \tag{12}$$

2) Mean relative deviation: D-factor (D = 0: perfect agreement)

$$D = \frac{1}{N}\sum_{i=1}^{N}\left|\frac{\sigma_i^{exp}-\sigma_i^{cal}}{\sigma_i^{exp}}\right| \tag{13}$$

3) Mean Ratio: R-factor (R = 1: perfect agreement on average)

$$R = \frac{1}{N}\sum_{i=1}^{N}\frac{\sigma_i^{cal}}{\sigma_i^{exp}}. \tag{14}$$

Here, σ_i^{exp} and σ_i^{cal} represents the experimental cross-section data obtained from the EXFOR database [5] [6] [15] [16] and the cross-sections calculated using

TALYS-2.0 for the corresponding experimental energy values, respectively, while N denotes the total number of experimental data points considered in the analysis. Within this statistical framework, the LDM yielding the value 1 for *F* and *R*, and 0 for *D* is considered to provide the best agreement between theoretical predictions and experimental observations [39]. The theoretical excitation functions across all investigated models were generated utilizing a discrete incident proton energy mesh with a uniform step size of 0.1 MeV starting from the respective reaction thresholds. To evaluate the statistical deviation factors, a linear interpolation procedure was implemented to extract precise cross-section values (σ_i^{cal}) and corresponding to the exact incident energy points of the experimental data (σ_i^{exp}).

The *F*-factor measures deviations on a logarithmic scale, capturing the overall trend of the excitation function. The *D*-factor gives the average relative difference between calculated and experimental values, while the *R*-factor compares values point by point, making it sensitive to local variations. Since each factor measures the agreement from a different perspective, they do not always identify the same model as the best fit. Among these metrics, the F-factor is considered the most appropriate for comparative analyses of different calculations, particularly when experimental data are limited [37].

2.4. SRIM-2013

The Stopping and Range of Ions in Matter (SRIM) code [40] is a Monte Carlo-based simulation package designed to study the stopping and range of ions in matter. It provides a set of computational tools for modeling various aspects of ion transport, with common applications in ion stopping, implantation, and transmission studies. In this work, the SRIM-2013 code was used to calculate the stopping power for proton-induced reaction on ^{169}Tm target over an energy range up to 200 MeV. The stopping power calculations are based on the Bethe-Bloch formula, which describes the mean energy loss per unit path length of charged particles as they traverse a material [40]. The original Bethe-Bloch relativistic stopping formula for a particle with speed v, charge z, and energy E, traveling a distance x into a target of electron number density n and mean excitation energy I is, in SI units:

$$S(E) = -\frac{\mathrm{d}E}{\mathrm{d}x} = \frac{nz^2e^4}{4\pi\epsilon_0^2\beta^2 m_e c^2}\left[\ln\left(\frac{2m_e v^2\beta^2}{I\cdot\left(1-\beta^2\right)}\right) - \beta^2\right] \tag{15}$$

where c is the speed of light and ϵ_0 the vacuum permittivity, $\beta = \frac{v}{c}$, e and m_e the electron charge and rest mass respectively. The electron density of the material n can be calculated by $n = \frac{N_A \cdot Z \cdot \rho}{A \cdot M_u}$, where ρ is the density of the material, Z its atomic number, A its relative atomic mass, N_A the Avogadro number and M_u the Molar mass constant.

2.5. Integral Yield of ^{169}Yb

Theoretical integral yields were determined for the production of ^{169}Yb radionuclide over an incident proton energy range up to 200 MeV. The yield calculation was based on the integration of reaction cross sections with the corresponding stopping power of the target material. The yield for ^{169}Yb was assessed through reaction ^{169}Tm(p, n). In this case, the integral yield was evaluated from the maximum incident energy down to the specific threshold energy of the reaction. The production cross sections were calculated using the TALYS-2.0 code with the Hauser–Feshbach nuclear model, while the stopping powers were derived from the SRIM-2013 code using Equation (8). The production yield of ^{169}Yb radionuclide was calculated using the excitation function [41] [42] as:

$$Y = H \cdot \frac{N_A}{A} \cdot I_p \cdot \left(1 - \mathrm{e}^{-\lambda t}\right) \cdot \int_{E_{\min}}^{E_{\max}} \frac{\sigma(E)}{S(E)} \mathrm{d}E \tag{16}$$

where Y is the activity (in Bq) of the ^{169}Yb, H is the isotope abundance of the target ^{169}Tm, $\sigma(E)$ is the energy-dependent reaction cross-section at energy E calculated from TALYS-2.0, I_p is the projectile current, $S(E)$ is the stopping power derived from SRIM-2013 code, λ is the decay constant of the product, and t is the time of irradiation.

3. Results and Discussion

The proton-induced reaction on ^{169}Tm was systematically investigated up to an incident proton energy of 200 MeV, considering the emission of α, n, d, t, and other possible reaction products. The excitation functions of the ^{169}Tm(p, n + α)^{165}Er, ^{169}Tm(p, α)^{166}Er, ^{169}Tm(p, ^{3}He)^{167}Er, ^{169}Tm(p, t)^{167}Tm, ^{169}Tm(p, n + p)^{168}Tm, ^{169}Tm(p, 4n)^{166}Yb, ^{169}Tm(p, 3n)^{167}Yb, ^{169}Tm(p, 2n)^{168}Yb, ^{169}Tm(p, n)^{169}Yb, and ^{169}Tm(p, γ)^{170}Yb reactions channels were evaluated using TALYS-2.0. The corresponding reaction threshold energies for these channels are listed in **Table 1**. A detailed discussion of the calculated excitation functions and cross-section characteristics for each reaction channel is presented in the following sections.

3.1. Excitation Functions of the ^{169}Tm(p, n + α)^{165}Er, ^{169}Tm(p, α)^{166}Er, ^{169}Tm(p, ^{3}He)^{167}Er, ^{169}Tm(p, t)^{167}Tm, ^{169}Tm(p, n + p)^{168}Tm, ^{169}Tm(p, 2n)^{168}Yb, and ^{169}Tm(p, γ)^{170}Yb Reactions

Figure 1 presents the TALYS-2.0 calculated excitation functions for seven proton-induced reaction channels on the monoisotopic target ^{169}Tm using CTM, BFM, GSM, SHFB, SHFB(C), and GHFB. Since no experimental cross-section data are currently available in the EXFOR database for these reaction channels, the calculated results were compared only with the TENDL-2023 evaluated nuclear data library. Overall, the six LDMs exhibit similar excitation function trends, indicating that the general reaction mechanisms are consistently reproduced by TALYS-2.0, although noticeable differences in magnitude emerge in specific energy regions.

For the ^{169}Tm(p, n + α)^{165}Er reaction (**Figure 1(a)**), the cross section rises rapidly above the reaction threshold and reaches values of approximately 20 - 35 mb in the intermediate-energy region. Several local maxima and minima are observed between 20 and 180 MeV, reflecting the competition between compound nucleus formation and pre-equilibrium particle emission. The GSM model predicts slightly larger cross sections over most of the energy range, whereas the microscopic models tend to produce lower values at higher energies.

A similar trend is observed for the ^{169}Tm(p, α)^{166}Er reaction (**Figure 1(b)**), where the excitation function exhibits a pronounced low-energy peak followed by a gradual increase toward intermediate energies. Beyond approximately 60 MeV, all models predict relatively stable cross sections with moderate model-dependent variations. The GHFB and SHFB(C) models generally yield larger cross sections in the high-energy region, suggesting a stronger sensitivity of α-particle emission to microscopic level-density descriptions.

The excitation function of the ^{169}Tm(p, ^{3}He)^{167}Er reaction (**Figure 1(c)**) shows a steep increase above threshold, followed by a broad plateau extending from approximately 60 to 160 MeV. The calculated cross sections remain within a relatively narrow range among the six LDMs, indicating that this reaction channel is less sensitive to the choice of LDM.

For the ^{169}Tm(p, t)^{167}Tm reaction (**Figure 1(d)**), the cross section increases sharply and attains values exceeding 200 mb in the 40 - 80 MeV region. A broad plateau is subsequently observed, followed by a gradual decline at higher energies. Among the investigated models, GHFB consistently predicts the largest cross sections, while CTM and SHFB yield comparatively lower values. The differences between the models become more pronounced above 100 MeV, where pre-equilibrium contributions dominate the reaction mechanism.

The ^{169}Tm(p, n + p)^{168}Tm reaction (**Figure 1(e)**) exhibits behavior similar to that of the ^{3}He-emission reaction. The excitation function rises rapidly after threshold and reaches a broad maximum between approximately 30 and 80 MeV. Thereafter, the cross section decreases gradually with increasing proton energy. The six LDMs produce very similar excitation functions, indicating that the calculated reaction probability is relatively insensitive to the level-density prescription. Nevertheless, the GHFB model again predicts slightly larger cross sections in the intermediate-energy region.

A distinctly different behavior is observed for the ^{169}Tm(p, 2n)^{168}Yb reaction (**Figure 1(f)**). The excitation function exhibits a well-defined peak near 15 - 20 MeV with cross sections approaching 103 mb, followed by a continuous decline toward higher proton energies. This trend is characteristic of neutron-emission reactions, where the reaction probability is highest near the optimum excitation energy and decreases as competing reaction channels become increasingly important.

Finally, the ^{169}Tm(p, γ)^{170}Yb reaction (**Figure 1(g)**) displays the smallest cross sections among all investigated channels. The excitation function reaches a

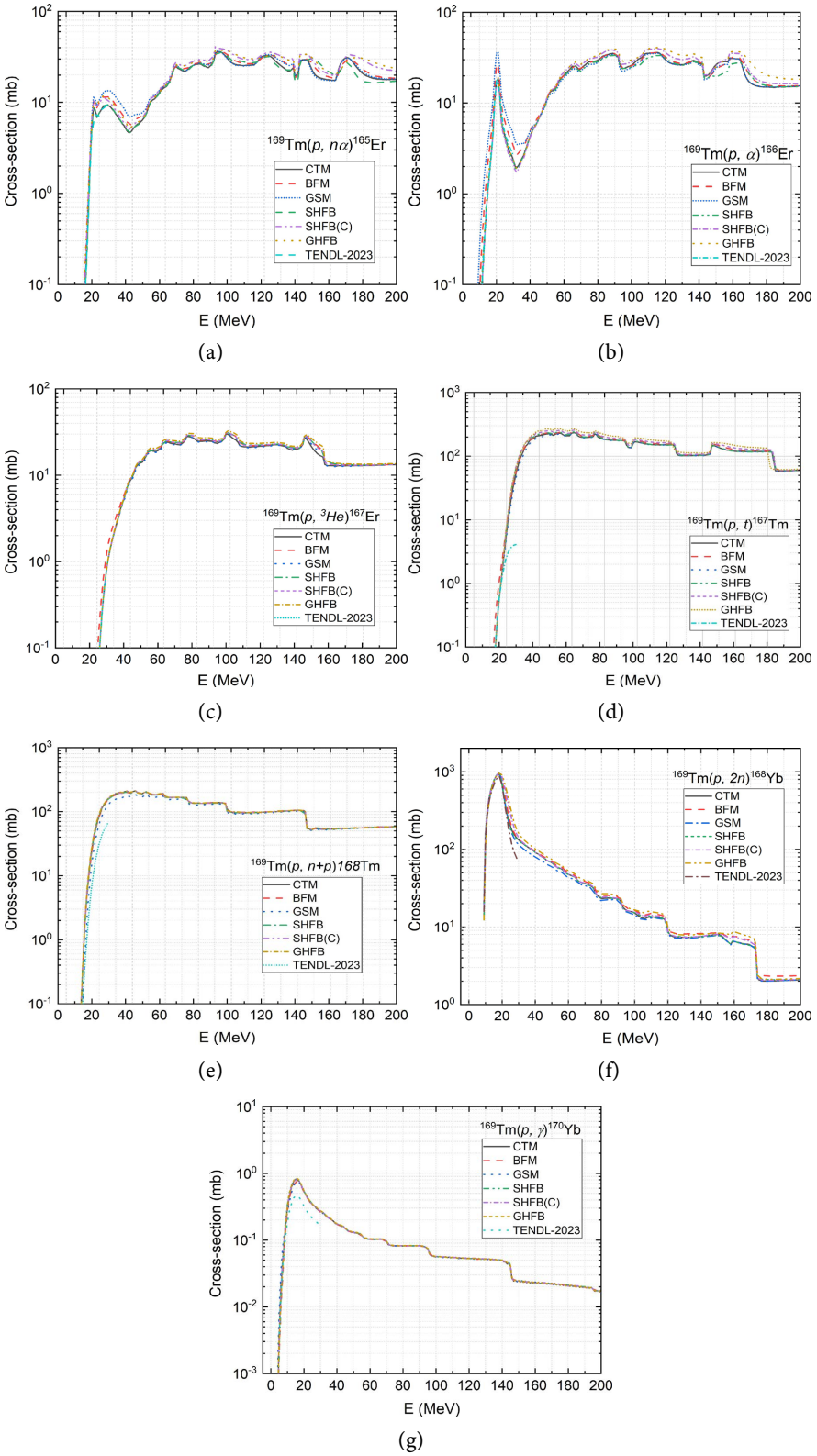

Figure 1. TALYS-2.0 calculated excitation function of the (a) ^{169}Tm(p, n + α)^{165}Er, (b) ^{169}Tm(p, α)^{166}Er, (c) ^{169}Tm(p, ^{3}He)^{167}Er, (d) ^{169}Tm(p, t)^{167}Tm, (e) ^{169}Tm(p, n + p)^{168}Tm, (f) ^{169}Tm(p, 2n)^{168}Yb, and (g) ^{169}Tm(p, γ)^{170}Yb reaction obtained using six nuclear LDMs over the proton energy range of 1 - 200 MeV.

maximum below 1 mb in the low-energy region and decreases steadily with increasing proton energy. The small magnitude of the cross section reflects the relatively low probability of radiative capture compared with charged-particle and neutron-emission processes. The calculated results from all six LDMs are nearly identical, indicating that this reaction channel is only weakly affected by variations in the level-density model.

Overall, the TALYS-2.0 calculations demonstrate that the selected LDMs provide consistent predictions for the investigated reaction channels. While CTM, BFM, and GSM generally reproduce the low-energy structures more closely to the TENDL-2023 evaluation, SHFB, SHFB(C), and GHFB tend to predict somewhat larger cross sections at higher proton energies. These theoretical results provide valuable nuclear data for reaction channels where experimental measurements are currently unavailable and may serve as useful guidance for future cross-section measurements and nuclear data evaluations.

3.2. ^{169}Tm(p, 4n)^{166}Yb Reaction

The experimental cross-section data for the ^{169}Tm(p, 4n)^{166}Yb reaction [5] [6], available in the EXFOR database, show generally similar trends over the investigated energy range, although some differences in magnitude and peak position are observed among the datasets. Most measurements indicate a reaction threshold near 25 MeV and a broad maximum around 35 - 40 MeV reaching a maximum cross-section of about 900 mb (see **Figure 2**). These variations may originate from differences in experimental conditions such as target thickness, proton beam-energy calibration, irradiation parameters, detector efficiency, and data analysis procedures. In many studies, the activation method followed by off-line γ-ray spectrometry was used for cross-section determination, where uncertainties associated with counting statistics, decay data, and overlapping γ-ray lines could contribute to the observed discrepancies. Nevertheless, the available experimental data exhibit an overall consistent excitation-function behavior for this reaction channel.

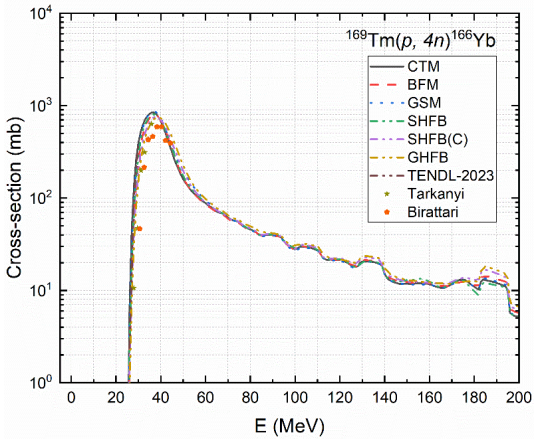

Figure 2. Excitation function of the ^{169}Tm(p, 4n)^{166}Yb reaction compared with experimental data [5] [6] from the EXFOR database and the TNDL-2023 evaluated nuclear data library [18].

To validate the nuclear LDMs employed in the TALYS-2.0 calculations, the statistical deviation factors *F*, *D*, *R* were evaluated using Equations (12)-(14). The calculated factors for the six LDMs and the available experimental datasets with the evaluated TENDL-2023 data [5] [6] [18] were summarized in **Table 2**.

Table 2. Statistical factors for different LDMs of ^{169}Tm(p, 4n)^{166}Yb reaction.

LDMs	^{169}Tm(p, 4n)^{166}Yb								
	TENDL-2023 [18]			Tárkányi *et al.* [6]			Birattari *et al.* [5]		
	F	*D*	*R*	*F*	*D*	*R*	*F*	*D*	*R*
CTM	1.60	0.48	1.48	5.53	6.20	7.20	2.37	1.38	2.37
BFM	1.61	0.36	0.63	3.65	3.14	4.14	2.11	1.05	2.05
GSM	**1.35**	0.28	1.15	4.81	4.93	5.94	2.33	1.33	2.33
SHFB	1.36	**0.21**	0.79	4.08	3.78	4.78	2.20	1.16	2.16
SHFB(C)	2.16	0.53	0.46	3.05	2.30	3.30	1.93	0.86	1.86
GHFB	3.03	0.66	**0.34**	**2.52**	**1.57**	**2.57**	**1.82**	**0.75**	**1.75**

The GSM and SHFB models exhibit lower *F* and *D* values with respect to the TENDL-2023 evaluation, indicating better agreement with the evaluated excitation functions, while their corresponding *R*-values remain close to unity, further confirming strong model consistency. In contrast, the GHFB model yields relatively larger deviation factors, indicating weaker agreement with the evaluated benchmark data. However, comparison with the experimental datasets reported by Birattari *et al.* [5] and Tárkányi *et al.* [6] reveals that the GHFB model produces the lowest *F*, *D* and *R*-factors, indicating superior predictive performance relative to the phenomenological models.

These results demonstrate that the agreement between theoretical TALYS-2.0 calculations and experimental observations strongly depends on the selected LDM and dataset, implying that no single LDM consistently outperforms the others over the entire energy range. The average values of the statistical deviation factors are presented in **Figure 3**.

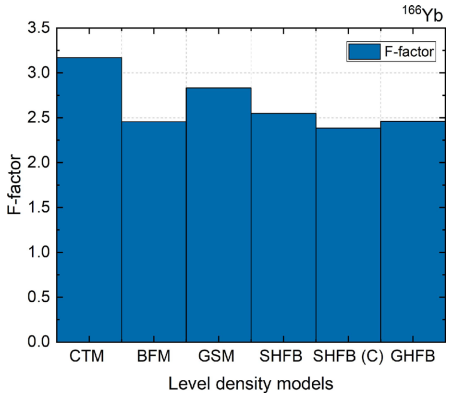

(a)

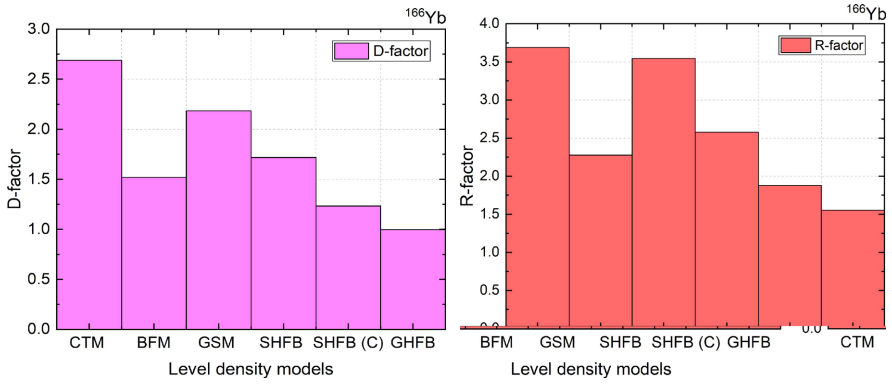

(b) (c)

Figure 3. Average values of the statistical deviation factors: (a) *F*-factor, (b) *D*-factor, and (c) *R*-factor calculated for the different LDMs, experimental data, and TENDL-2023 evolution for the ^{169}Tm(p, 4n)^{166}Yb reaction.

3.3. ^{169}Tm(p, 3n)^{167}Yb Reaction

Figure 4 presents the excitation function of the ^{169}Tm(p, 3n)^{167}Yb reaction calculated using TALYS-2.0, together with the available experimental data and the TENDL-2023 evaluated library for comparison. Experimental cross-section datasets are available in the EXFOR database from Tárkányi *et al.* [6] for the proton energy range 24.5 - 35.8 MeV and from Birattari *et al.* [5] for 19.7 - 42.5 MeV, while the TENDL-2023 evaluated data cover the 18 - 30 MeV energy region [18]. In the present work, the excitation function was extended up to 200 MeV incident proton energy. The reaction channel opens at approximately ~18 MeV, marking the threshold energy. Following the threshold, the cross section increases rapidly and reaches a maximum of 1039 mb at 26 MeV. This peak corresponds to the optimal excitation energy of the compound nucleus. Beyond the peak region, the cross section gradually decreases with increasing proton energy, where pre-equilibrium emission effects may contribute significantly to the reaction mechanism at higher energies.

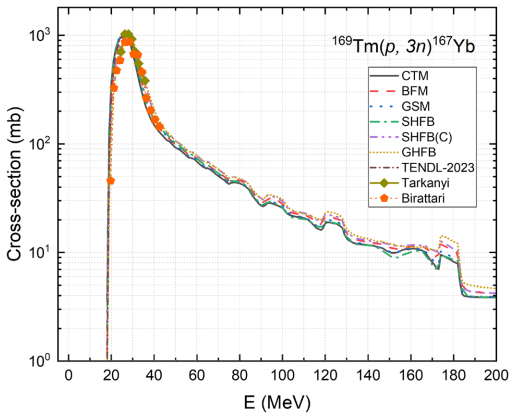

Figure 4. Excitation function of the ^{169}Tm(p, 3n)^{167}Yb reaction compared with experimental data [5] [6] from the EXFOR database and the TNDL-2023 evaluated nuclear data library [18].

The statistical deviation factors *F*, *D* and *R*, summarized in Table 3, were evaluated to validate the performance of the six nuclear LDMs. The BFM and SHFB models produce the lowest *F* and *D* values relative to the TENDL-2023 evaluation. Their corresponding *R*-values also remain close to unity, confirming reliable predictive capability. In contrast, comparison with the experimental datasets of Birattari *et al.* [5] and Tárkányi *et al.* [6] indicates that the SHFB(C) and GHFB models provide comparatively lower statistical deviation factors, suggesting improved agreement with measured cross sections. Although the CTM and BFM models yield favorable *R*-values for some datasets, the microscopic SHFB(C) and GHFB approaches generally demonstrate better consistency with the experimental observations. Overall, the phenomenological models remain effective in reproducing the evaluated excitation functions, whereas the microscopic models provide improved agreement with the available experimental data. The average values of the statistical deviation factors are presented in Figure 5.

3.4. ^{169}Tm(p, n)^{169}Yb Reaction

The excitation function of the ^{169}Tm(p, n)^{169}Yb reaction was calculated using TALYS-2.0 with different nuclear LDMs from the reaction threshold up to 200 MeV incident proton energy. The present work provides an extended cross-section profile over a broad energy range, whereas the available experimental

Table 3. Statistical factors for different LDMs of ^{169}Tm(p, 3n)^{167}Yb reaction.

LDMs	^{169}Tm(p, 3n)^{167}Yb								
	TENDL-2023 [18]			Tárkányi *et al.* [6]			Birattari *et al.* [5]		
	F	*D*	*R*	*F*	*F*	*D*	*R*	*D*	*F*
CTM	1.55	0.38	1.34	1.31	0.20	**0.83**	1.50	0.38	1.16
BFM	**1.17**	**0.10**	0.92	1.13	0.09	0.93	1.32	0.24	**1.15**
GSM	1.43	0.28	1.27	1.15	0.11	0.95	1.45	0.32	1.25
SHFB	1.25	0.15	1.146	1.18	0.12	0.92	1.44	0.33	1.22
SHFB (C)	1.30	0.19	0.90	**1.04**	**0.04**	1.00	1.24	0.21	1.19
GHFB	1.74	0.32	**0.72**	1.08	0.07	1.02	**1.19**	**0.17**	1.17

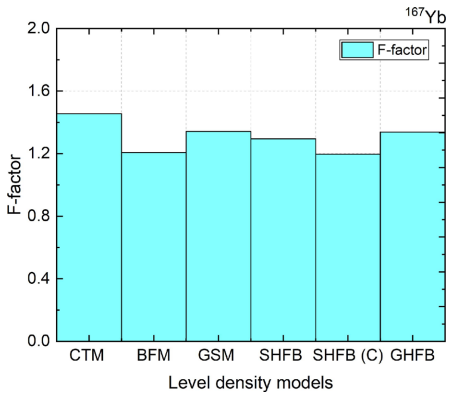

(a)

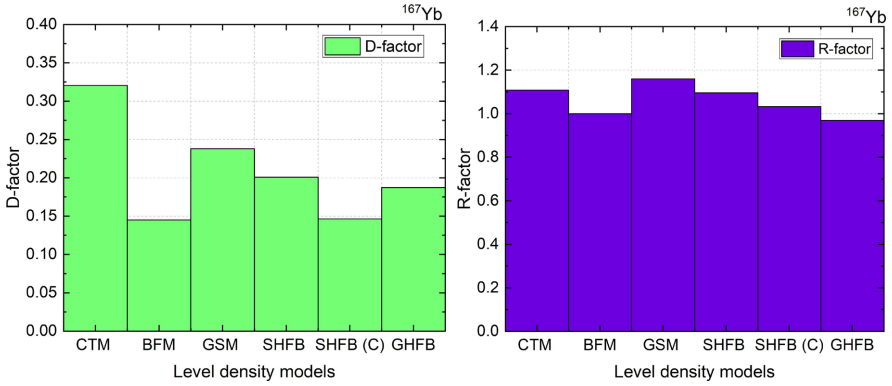

(b) (c)

Figure 5. Average values of the statistical deviation factors: (a) *F*-factor, (b) *D*-factor, and (c) *R*-factor calculated for the different LDMs, experimental data, and TENDL-2023 evolution for the ^{169}Tm(p, 3n)^{167}Yb reaction.

measurements are limited to lower proton energies. Among the investigated models, the GHFB model predicts the maximum cross section of approximately 170 mb at around 10 MeV. All LDMs exhibit similar excitation function trends throughout the investigated energy range, with only minor deviations in the peak magnitudes and high-energy behavior. The CTM model predicts comparatively higher cross-section values at elevated proton energies than the other LDMs.

Figure 6 compares the TALYS-2.0 calculated excitation functions, particularly the GHFB results, with the available experimental datasets. Experimental measurements by Spahn *et al.* [15] cover the proton energy range from 4.8 to 44.9 MeV, with the maximum cross section observed near 11 MeV. Tárkányi *et al.* [6] extended the investigation of proton-induced reactions on ^{169}Tm within the 24.5 - 35.8 MeV energy range. Saito *et al.* [16] measured the excitation function up to 17.5 MeV, providing detailed low-energy data between 5.3 and 17.5 MeV that clearly describe

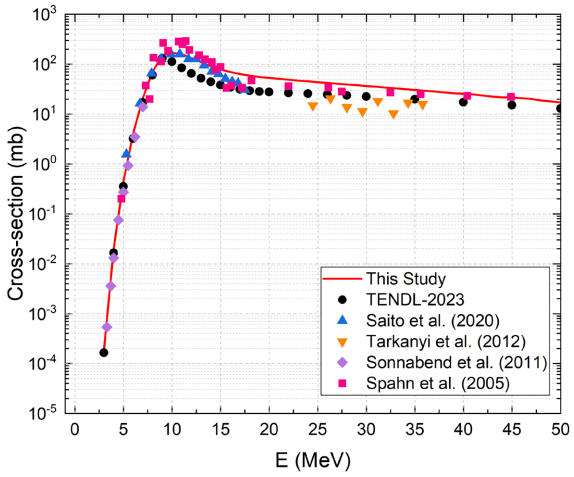

Figure 6. Excitation function of the ^{169}Tm(p, n)^{169}Yb reaction compared with experimental data [6] [15] [16] [43] from the EXFOR database and the TENDL-2023 evaluated nuclear data library [18].

the threshold and peak behavior. In addition, Sonnabend *et al.* [43] investigated the reaction in the context of astrophysical p-process nucleosynthesis, performing measurements at very low proton energies between 3.3 and 7.0 MeV corresponding to the Gamow window relevant to stellar environments.

The statistical factor analysis of the ^{169}Tm(p, n)^{169}Yb reaction cross sections was performed to evaluate the predictive performance of different nuclear LDMs against available experimental datasets and the TENDL-2023 [18] evaluated library. The calculated *F*-, *D*- and *R*-factors are summarized in **Table 4**. Among the investigated models, the microscopic approaches, particularly the SHFB and SHFB(C) models, generally produce lower *F*, *D* and *R* values for the TENDL-2023 evaluation and the experimental datasets reported by Spahn *et al.* [15] and Tárkányi *et al.* [6], indicating comparatively better agreement with the measured cross sections in the low-energy region. In contrast, the GSM and CTM models yield lower statistical deviation factors for the experimental data of Sonnabend *et al.* [43], while the BFM model provides the lowest *F* and *D* values for the dataset reported by Saito *et al.* [16].

Table 4. Statistical factors for different LDMs of ^{169}Tm(p, n)^{169}Yb reaction.

^{169}Tm(p, n)^{169}Yb															
LDMs	TENDL-2023 [18]			Saito *et al.* [16]			Tárkányi *et al.* [6]			Sonnabend *et al.* [43]			Spahn *et al.* [15]		
	F	*D*	*R*	*F*	*D*	*R*	*F*	*D*	*R*	*F*	*D*	*R*	*F*	*D*	*R*
CTM	1.52	0.44	1.36	1.32	0.21	0.94	2.70	1.70	2.70	1.63	0.63	1.63	2.15	0.40	1.12
BFM	1.62	0.57	1.53	**1.21**	0.16	1.02	2.94	1.95	2.95	1.64	0.64	1.64	2.16	0.47	1.23
GSM	1.61	0.53	1.45	1.23	0.18	1.11	2.72	1.72	2.71	**1.62**	**0.61**	**1.61**	2.10	0.39	1.17
SHFB	**1.41**	**0.34**	**1.26**	1.24	**0.15**	**0.92**	2.35	1.33	2.33	1.64	0.63	1.64	2.07	**0.28**	**0.99**
SHFB(C)	1.43	0.36	1.28	1.24	0.17	0.95	**2.33**	**1.32**	**2.32**	1.63	0.63	1.63	2.07	0.29	1.00
GHFB	1.58	0.49	1.41	1.24	0.18	1.14	2.45	1.40	2.44	1.63	0.63	1.63	**2.04**	0.30	1.09

The R-values remain close to unity for most models, suggesting that the overall normalization of the TALYS-2.0 predictions is reasonable despite variations in absolute deviations. However, the dataset of Tárkányi *et al.* [6] exhibits comparatively larger F and D values across all LDMs, which may reflect experimental uncertainties or limitations in reproducing the corresponding excitation functions. Overall, the analysis indicates that no single LDM provides universal agreement for all experimental datasets, although the microscopic SHFB and SHFB(C) models demonstrate the most consistent overall performance. The average values of the statistical deviation factors are shown in **Figure 7**.

3.5. Production Yield of ^{169}Yb

Figure 8 illustrates the time evolution of the activity and production amount of ^{169}Yb calculated using six different nuclear LDMs. These production parameters were evaluated using the monoisotopic ^{169}Tm target geometry described in

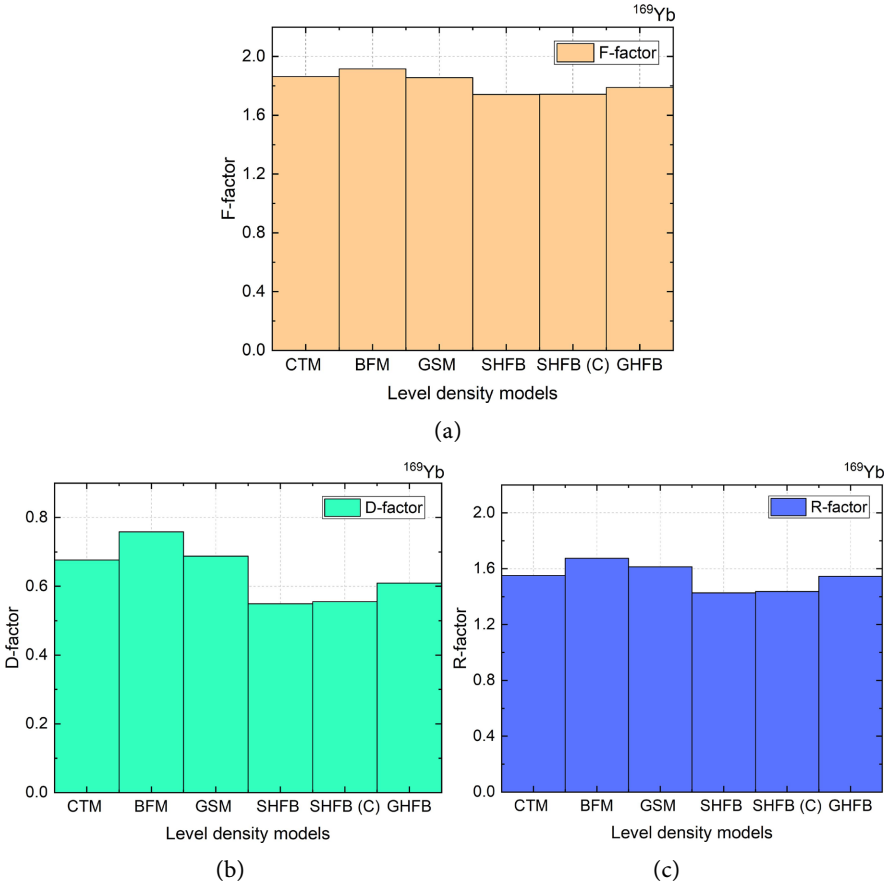

Figure 7. Average values of the statistical deviation factors: (a) *F*-factor, (b) *D*-factor, and (c) *R*-factor calculated for the different LDMs, experimental data, and TENDL-2023 evolution for the ^{169}Tm(p, n)^{169}Yb reaction.

Section 2.2. During the 24-h irradiation period, both quantities increase continuously due to the ongoing production of ^{169}Yb. The activity exhibits an approximately linear increase and reaches its maximum value of approximately 880 GBq at EOB, after which it gradually decreases during the cooling period as a consequence of radioactive decay. The accumulated production amount follows a similar trend during irradiation, increasing rapidly and attaining its highest value at EOB. Following the cessation of irradiation, the production amount decreases only slightly over the 24 h cooling period because of the relatively long half-life of ^{169}Yb. Among the investigated LDMs, the BFM model predicts the highest activity and production amount, whereas the SHFB model yields the lowest values. Although the GHFB model predicts a larger absolute peak cross section at its maximum, the BFM model exhibits a broader excitation function profile with a significantly larger integrated low-energy cross-section area across the near-threshold domain, which ultimately drives its higher cumulative thick-target yield and activity calculations. Nevertheless, the differences among the six models remain moderate, indicating a high degree of consistency in the predicted production characteristics. The maximum production amount at EOB is approximately 3.5 ×

10^{18} atoms for the BFM model. After EOB, a gradual decrease in production is observed, reducing the yield to approximately 3.42×10^{18} atoms during the cooling period. Overall, a moderate but consistent variation is observed among all LDMs, indicating the stability and reliability of the theoretical predictions for accelerator-based ^{169}Yb production.

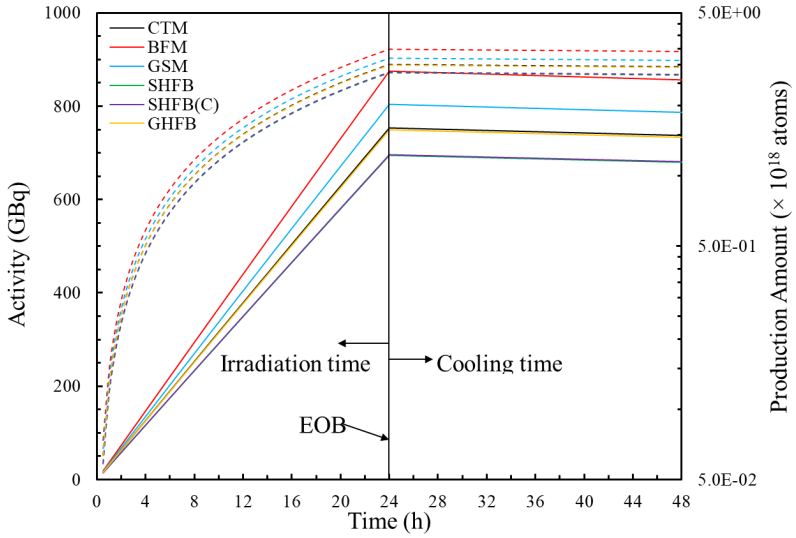

Figure 8. Time-dependent activity (solid line, left axis) and production amount (dashed lines, right axis) of ^{169}Yb calculated using six nuclear LDMs as a function of irradiation + cooling time. The vertical black line indicated the EOB at 24 h, separating the irradiation and cooling periods.

Furthermore, the calculated integral yield of ^{169}Yb is shown in **Figure 9** as a function of incident proton energy for a monoisotopic ^{169}Tm target. The yield increased significantly with increasing proton energy. Although the maximum cross-section of the ^{169}Tm(p, n)^{169}Yb reaction occurs near 11 MeV, the overall yield continues to rise significantly with increasing incident proton energy. This behavior reflects the cumulative nature of thick-target yields. Higher-energy beams contribute additional reaction events across the full energy range down to the threshold, leading to a steep increase in yield up to about 60 MeV and a slower rise thereafter. The curve eventually approaches a plateau at high energies, indicating fading returns due to competing reaction channels and reduced efficiency. However, from a practical medical production standpoint, selecting an optimum irradiation window requires balancing this maximum yield against strict radionuclidic purity constraints. While higher proton energies maximize the total integral yield, they simultaneously trigger competing multi-neutron emission channel, specifically ^{169}Tm(p, 2n)^{168}Yb, ^{169}Tm(p, 3n)^{167}Yb and ^{169}Tm(p, 4n)^{166}Yb. Because the co-produced ^{168}Yb contaminant is a stable isotope (**Table 1**), it acts as an inseparable isotopic carrier that permanently reduces the specific activity of ^{169}Yb, making impurity suppression a primary limiting constraint alongside the peak cross-section values.

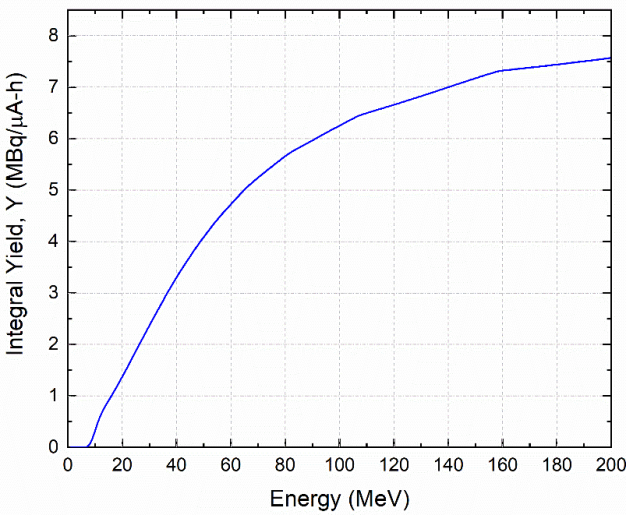

Figure 9. Integral yield of ^{169}Yb as a function of incident proton energy.

For the energy interval of 15 → 8 MeV, the calculated physical thick-target yield of ^{169}Yb was found to be 0.912 MBq/μA-h. This value is approximately 41.80% higher than the experimental yield of 0.643 ± 0.050 MBq/μA-h reported by Nadi *et al.* [44], who produced ^{169}Yb by irradiating a Tm_2O_3 target with 15 MeV protons at a beam current of 20 μA for 20 min using the AMIRS (Cyclone-30, IBA, Belgium) cyclotron. The difference between the calculated and measured yields may arise from target composition, energy degradation within the target, irradiation geometry, beam-loss effects, and other experimental factors that are not fully accounted for in the theoretical model. Nevertheless, the reasonable agreement between the calculated and experimental yields supports the reliability of the TALYS-2.0 predictions.

4. Conclusions

In the present work, a comprehensive theoretical investigation of proton-induced reactions on ^{169}Tm was performed using the TALYS-2.0 nuclear reaction code over the incident proton energy range of 1-200 MeV. Excitation functions were calculated for the ^{169}Tm(p, n + α)^{165}Er, ^{169}Tm(p, α)^{166}Er, ^{169}Tm(p, ^{3}He)^{167}Er, ^{169}Tm(p, t)^{167}Tm, ^{169}Tm(p, n + p)^{168}Tm, ^{169}Tm(p, 4n)^{166}Yb, ^{169}Tm(p, 3n)^{167}Yb, ^{169}Tm(p, 2n)^{168}Yb, ^{169}Tm(p, n)^{169}Yb, and ^{169}Tm(p, γ)^{170}Yb reaction channels using six nuclear LDMs: CTM, BFM, GSM, SHFB, SHFB(C), and GHFB. The results demonstrate that the choice of LDM has a significant impact on the predicted cross sections, particularly at higher proton energies. In general, CTM, BFM, and GSM reproduce the low-energy excitation function behavior and the TENDL-2023 evaluated data more effectively, whereas SHFB, SHFB(C), and GHFB exhibit larger deviations at higher energies.

For the reaction channels with available experimental data, namely ^{169}Tm(p, 4n)^{166}Yb, ^{169}Tm(p, 3n)^{167}Yb, and ^{169}Tm(p, n)^{169}Yb, *F*-, *D*- and *R*-factor were employed to assess model performance. The analysis revealed that no single LDM

consistently provides the best agreement across all datasets. While CTM, BFM, and GSM generally show better consistency with the TENDL-2023 data, the SHFB and SHFB(C) models often exhibit improved agreement with experimental measurements, highlighting the importance of model selection in nuclear reaction calculations.

Particular emphasis was placed on the production of the therapeutic radionuclide ^{169}Yb through the ^{169}Tm(p, n)^{169}Yb reaction. The calculated excitation function indicates an optimal production window in the low-energy region, with a peak cross section occurring near 11 MeV. Production calculations further demonstrate the feasibility of accelerator-based ^{169}Yb generation. Among the investigated LDMs, the BFM model yielded the highest activity, production amount, and yield, despite the GHFB model predicting larger cross-section values. The time-dependent activity and yield profiles followed the expected growth-and-decay behavior of ^{169}Yb, confirming the suitability of this production route for practical applications.

Finally, this study provides valuable nuclear data for proton-induced reactions on 169Tm and demonstrates the influence of nuclear level density modeling on reaction predictions. The results support the development of reliable accelerator-based production strategies for ^{169}Yb and contribute to the improvement of evaluated nuclear data libraries. Future experimental measurements, particularly for reaction channels lacking EXFOR data and in energy regions where significant model discrepancies exist, are recommended to further validate and refine the theoretical predictions.

Acknowledgements

The authors would like to express their sincere gratitude to Mr. Md. Masum Billah, graduate researcher of Toyohashi University of Technology, Japan for his valuable support and assistance in providing relevant literature and published data used in this study.

Conflicts of Interest

The authors declare no conflicts of interest regarding the publication of this paper.

References

[1] Ruth, T. (2009) Accelerating Production of Medical Isotopes. *Nature*, **457**, 536-537. https://doi.org/10.1038/457536a

[2] Khandaker, M.U., Uddin, M.S., Kim, K., Lee, M.W., Kim, K.S., Lee, Y.S., *et al.* (2008) Excitation Functions of Proton Induced Nuclear Reactions on NatW up to 40 MeV. *Nuclear Instruments and Methods in Physics Research Section B: Beam Interactions with Materials and Atoms*, **266**, 1021-1029. https://doi.org/10.1016/j.nimb.2008.02.037

[3] (2026) Table of Nuclides—Nuclear Structure and Decay Data, IAEA Nuclear Data Section. https://nds.iaea.org/relnsd/vcharthtml/VChartHTML.html

[4] Otuka, N., Dupont, E., Semkova, V., Pritychenko, B., Blokhin, A.I., Aikawa, M., *et al.*

(2014) Towards a More Complete and Accurate Experimental Nuclear Reaction Data Library (EXFOR): International Collaboration between Nuclear Reaction Data Centres (NRDC). *Nuclear Data Sheets*, **120**, 272-276. https://doi.org/10.1016/j.nds.2014.07.065

[5] Birattari, C., Gadloli, E., Erba, E.G., Strini, A.M.G., Strini, G. and Tagliaferri, G. (1973) Pre-Equilibrium Processes in (p,n) Reactions. *Nuclear Physics A*, **201**, 579-592. https://doi.org/10.1016/0375-9474(73)90322-9

[6] Tárkányi, F., Hermanne, A., Takács, S., Ditrói, F., Spahn, I. and Ignatyuk, A.V. (2012) Activation Cross-Sections of Proton Induced Nuclear Reactions on Thulium in the 20-45MeV Energy Range. *Applied Radiation and Isotopes*, **70**, 309-314. https://doi.org/10.1016/j.apradiso.2011.08.020

[7] Patel, N.S., Fan, P., Chiu-Tsao, S., Ravi, K., Sherman, W., Quon, H., *et al.* (2001) Yt-terbium-169: A Promising New Radionuclide for Intravascular Brachytherapy. *Cardiovascular Radiation Medicine*, **2**, 173-180. https://doi.org/10.1016/s1522-1865(01)00085-3

[8] Robitaille, M., Ménard, C., Famulari, G., Béliveau-Nadeau, D. and Enger, S.A. (2024) ^{169}Yb-Based High Dose Rate Intensity Modulated Brachytherapy for Focal Treatment of Prostate Cancer. *Brachytherapy*, **23**, 523-534. https://doi.org/10.1016/j.brachy.2024.05.005

[9] Leonard, K.L., DiPetrillo, T.A., Munro, J.J. and Wazer, D.E. (2011) A Novel Ytterbium-169 Brachytherapy Source and Delivery System for Use in Conjunction with Minimally Invasive Wedge Resection of Early-Stage Lung Cancer. *Brachytherapy*, **10**, 163-169. https://doi.org/10.1016/j.brachy.2010.06.006

[10] Mason, D.L.D., Battista, J.J., Barnett, R.B. and Porter, A.T. (1992) Ytterbium-169: Calculated Physical Properties of a New Radiation Source for Brachytherapy. *Medical Physics*, **19**, 695-703. https://doi.org/10.1118/1.596813

[11] Yamabayashi, H. (1994) Development of Production Techniques for Ytterbium-169 Sources. *Radioisotopes*, **43**, 296-308. https://doi.org/10.3769/radioisotopes.43.296

[12] Saxena, S.K., Kumar, Y., Jagadeesan, K.C., Nuwad, J., Bamankar, Y.R. and Dash, A. (2015) Studies on the Development of ^{169}Yb-Brachytherapy Seeds: New Generation Brachytherapy Sources for the Management of Cancer. *Applied Radiation and Isotopes*, **101**, 75-82. https://doi.org/10.1016/j.apradiso.2015.03.020

[13] DeLand, F.H., *et al.* (1971) Cisternography with ^{169}Yb-DTPA. *Journal of Nuclear Medicine*, **12**, 683-689. https://jnm.snmjournals.org/content/jnumed/12/10/683.full.pdf

[14] Naz, A., Amjed, N., Wajid, A.M., Khan, S., Eman, M. and Chen, D. (2026) Evaluated Nuclear Data for the Optimum Cyclotron Production of ^{169}Yb. *Radiation Physics and Chemistry*, **248**, Article ID: 114063. https://doi.org/10.1016/j.radphyschem.2026.114063

[15] Spahn, I., Takács, S., Shubin, Y.N., Tárkányi, F., Coenen, H.H. and Qaim, S.M. (2005) Cross-Section Measurement of the ^{169}Tm(p,n) Reaction for the Production of the Therapeutic Radionuclide ^{169}Yb and Comparison with Its Reactor-Based Generation. *Applied Radiation and Isotopes*, **63**, 235-239. https://doi.org/10.1016/j.apradiso.2005.03.006

[16] Saito, M., Aikawa, M., Murata, T., Komori, Y., Haba, H., Takács, S., *et al.* (2020) Production Cross Sections of ^{169}Yb by the Proton-Induced Reaction on ^{169}Tm. *Nuclear Instruments and Methods in Physics Research Section B: Beam Interactions with Materials and Atoms*, **471**, 13-16. https://doi.org/10.1016/j.nimb.2020.03.019

[17] Koning, A., Hilaire, S. and Goriely, S. (2023) TALYS: Modeling of Nuclear Reactions.

The European Physical Journal A, **59**, Article No. 131.
https://doi.org/10.1140/epja/s10050-023-01034-3

[18] Koning, A.J., Rochman, D., Sublet, J.C., Dzysiuk, N., Fleming, M. and van der Marck, S. (2019) TENDL: Complete Nuclear Data Library for Innovative Nuclear Science and Technology. *Nuclear Data Sheets*, **155**, 1-55.
https://doi.org/10.1016/j.nds.2019.01.002

[19] (2026) Q-Value Calculator (QCalc). National Nuclear Data Center, Brookhaven National Laboratory. https://www.nndc.bnl.gov/qcalc/

[20] Raynal, J. (2007) ECIS-06, Coupled Channel, Statistical Model, Schrödinger and Dirac Equation, Dispersion Relation. NEA-0850/18 ECIS-06.

[21] Koning, A.J. and Delaroche, J.P. (2003) Local and Global Nucleon Optical Models from 1 KeV to 200 MeV. *Nuclear Physics A*, **713**, 231-310.
https://doi.org/10.1016/s0375-9474(02)01321-0

[22] Goriely, S., Hilaire, S., Girod, M. and Péru, S. (2016) The Gogny-Hartree-Fock-Bogoliubov Nuclear-Mass Model. *The European Physical Journal A*, **52**, Article No. 202.
https://doi.org/10.1140/epja/i2016-16202-3

[23] Sen'kov, R. and Zelevinsky, V. (2016) Nuclear Level Density: Shell-Model Approach. *Physical Review C*, **93**, Article ID: 064304.
https://doi.org/10.1103/physrevc.93.064304

[24] Gilbert, A. and Cameron, A.G.W. (1965) A Composite Nuclear-Level Density Formula with Shell Corrections. *Canadian Journal of Physics*, **43**, 1446-1496.
https://doi.org/10.1139/p65-139

[25] Plyaskin, V.I. and Kosilov, R.A. (2000) Level-Density Parameters in the Back-Shifted Fermi Gas Model. *Physics of Atomic Nuclei*, **63**, 752-757.
https://doi.org/10.1134/1.855702

[26] Dilg, W., Schantl, W., Vonach, H. and Uhl, M. (1973) Level Density Parameters for the Back-Shifted Fermi Gas Model in the Mass Range $40 < A < 250$. *Nuclear Physics A*, **217**, 269-298. https://doi.org/10.1016/0375-9474(73)90196-6

[27] Grossjean, M.K. and Feldmeier, H. (1985) Level Density of a Fermi Gas with Pairing Interactions. *Nuclear Physics A*, **444**, 113-132.
https://doi.org/10.1016/0375-9474(85)90294-5

[28] Demetriou, P. and Goriely, S. (2001) Microscopic Nuclear Level Densities for Practical Applications. *Nuclear Physics A*, **695**, 95-108.
https://doi.org/10.1016/s0375-9474(01)01095-8

[29] Ignatyuk, A.V., *et al.* (1979) Role of the Collective Effects in a Systematics of Nuclear Level Density. *Yadernaya Fizika*, **29**, 875-883.
https://inis.iaea.org/records/64xas-6sx16

[30] Ignatyuk, A.V., Weil, J.L., Raman, S. and Kahane, S. (1993) Density of Discrete Levels in ^{116}Sn. *Physical Review C*, **47**, 1504-1513. https://doi.org/10.1103/physrevc.47.1504

[31] Capote, R., Herman, M., Obložinský, P., Young, P.G., Goriely, S., Belgya, T., *et al.* (2009) RIPL—Reference Input Parameter Library for Calculation of Nuclear Reactions and Nuclear Data Evaluations. *Nuclear Data Sheets*, **110**, 3107-3214.
https://doi.org/10.1016/j.nds.2009.10.004

[32] Pearson, J.M., Goriely, S. and Samyn, M. (2002) A Hartree-Fock Nuclear Mass Formula. *The European Physical Journal A*, **15**, 13-16.
https://doi.org/10.1140/epja/i2001-10215-y

[33] Goriely, S., Hilaire, S. and Koning, A.J. (2008) Improved Microscopic Nuclear Level Densities within the Hartree-Fock-Bogoliubov Plus Combinatorial Method. *Physical*

Review C, **78**, Article ID: 064307. https://doi.org/10.1103/physrevc.78.064307

[34] Hilaire, S., Girod, M., Goriely, S. and Koning, A.J. (2012) Temperature-Dependent Combinatorial Level Densities with the D1M Gogny Force. *Physical Review C*, **86**, Article ID: 064317. https://doi.org/10.1103/physrevc.86.064317

[35] Saito, M., Aikawa, M., Komori, Y., Haba, H. and Takács, S. (2017) Production Cross Sections of ^{169}Yb and Tm Isotopes in Deuteron-Induced Reactions on ^{169}Tm. *Applied Radiation and Isotopes*, **125**, 23-26. https://doi.org/10.1016/j.apradiso.2017.04.010

[36] Kurenkov, N.V., Lunev, V.P. and Shubin, Y.N. (1999) Evaluation of Calculation Methods for Excitation Functions for Production of Radioisotopes of Iodine, Thallium and Other Elements. *Applied Radiation and Isotopes*, **50**, 541-549. https://doi.org/10.1016/s0969-8043(98)00048-7

[37] Broeders, C.H.M. and Konobeyev, A.Y. (2005) Improvement in Simulation of Equilibrium Particle Emission Using Intranuclear Cascade Evaporation Model. *Nuclear Instruments and Methods in Physics Research Section A*: *Accelerators*, *Spectrometers*, *Detectors and Associated Equipment*, **550**, 241-247. https://doi.org/10.1016/j.nima.2005.06.022

[38] Rahman, A.K.M.R. and Zubair, M.A. (2020) Cross Sections of ^{56}Fe(n, p)^{56}Mn, ^{55}Mn(n, p)^{55}Cr, ^{52}Cr(n, p)^{52}V, ^{56}Fe(n, α)^{53}Cr, ^{55}Mn(n, α)^{52}V and ^{52}Cr(n, α)^{49}Ti Reactions Using Phenomenological Level Density Models from Threshold to 20 MeV. *Applied Radiation and Isotopes*, **166**, Article ID: 109429. https://doi.org/10.1016/j.apradiso.2020.109429

[39] Hasan, K. and Rahman, A.K.M.R. (2026) Systematic Study of Deuteron Induced Reaction Cross Sections on ^{24}Mg and ^{27}Al Nuclei up to 50 MeV. *Applied Radiation and Isotopes*, **227**, Article ID: 112305. https://doi.org/10.1016/j.apradiso.2025.112305

[40] Ziegler, J.F., Ziegler, M.D. and Biersack, J.P. (2010) SRIM—The Stopping and Range of Ions in Matter (2010). *Nuclear Instruments and Methods in Physics Research Section B*: *Beam Interactions with Materials and Atoms*, **268**, 1818-1823. https://doi.org/10.1016/j.nimb.2010.02.091

[41] Sharifian, M., Sadeghi, M., Alirezapour, B., Yarmohammadi, M. and Ardaneh, K. (2017) Modeling and Experimental Data of Zirconium-89 Production Yield. *Applied Radiation and Isotopes*, **130**, 206-210. https://doi.org/10.1016/j.apradiso.2017.09.044

[42] Qaim, S.M. (2011) Cyclotron Production of Medical Radionuclides. In: Vértes, A., Nagy, S., Klencsár, Z., Lovas, R.G. and Rösch, F., Eds., *Handbook of Nuclear Chemistry*, Springer, 1903-1933. https://doi.org/10.1007/978-1-4419-0720-2_39

[43] Sonnabend, K., Glorius, J., Görres, J., Knörzer, M., Müller, S., Sauerwein, A., *et al.* (2011) Activation Experiments for *p*-Process Nucleosynthesis. *Journal of Physics*: *Conference Series*, **312**, Article ID: 042007. https://doi.org/10.1088/1742-6596/312/4/042007

[44] Nadi, H., Sadeghi, M., Enferadi, M. and Sarabadani, P. (2011) Cyclotron Production of ^{169}Yb: A Potential Radiolanthanide for Brachytherapy. *Journal of Radioanalytical and Nuclear Chemistry*, **289**, 361-365. https://doi.org/10.1007/s10967-011-1108-9